

# Development and Demonstration of a ReaxFF Reactive Force Field for Ni-Doped MoS<sub>2</sub>

Karen Mohammadtabar,<sup>†</sup> Enrique Guerrero,<sup>‡</sup> Sergio Romero Garcia,<sup>†</sup> Yun Kyung Shin,<sup>¶</sup> Adri C. T. van Duin,<sup>¶</sup> David A. Strubbe,<sup>‡</sup> and Ashlie Martini<sup>\*,†</sup>

<sup>†</sup>*Department of Mechanical Engineering, University of California Merced, 5200 N. Lake Road, Merced, California 95343, United States*

<sup>‡</sup>*Department of Physics, University of California Merced, 5200 N. Lake Road, Merced, California 95343, United States*

<sup>¶</sup>*Department of Mechanical Engineering, Pennsylvania State University, University Park, Pennsylvania 16802, United States*

E-mail: amartini(at)ucmerced.edu

## Abstract

The properties of MoS<sub>2</sub> can be tuned or optimized through doping. In particular, Ni doping has been shown to improve the performance of MoS<sub>2</sub> for various applications, including catalysis and tribology. To enable investigation of Ni-doped MoS<sub>2</sub> with reactive molecular dynamics simulations, we developed a new ReaxFF force field to describe this material. The force field parameters were optimized to match a large set of density-functional theory (DFT) calculations of 2H-MoS<sub>2</sub> doped with Ni, at four different sites (Mo-substituted, S-substituted, octahedral intercalation, and tetrahedral intercalation), under uniaxial, biaxial, triaxial, and shear strain. The force field was evaluated by comparing ReaxFF- and DFT-relaxed structural parameters and the tetrahedral/octahedral energy difference in doped 2H, energies of doped 1H and 1T monolayers, and doped 2H structures with vacancies. We demonstrated the force field with reactive simulations of sputtering deposition and annealing of Ni-doped MoS<sub>2</sub> films. Results show that the developed force field can accurately model the phase transition of Ni-doped MoS<sub>2</sub> from amorphous to crystalline. The newly developed force field can be used in subsequent investigations to study the properties and behavior of Ni-doped MoS<sub>2</sub> using reactive molecular dynamics simulations.

## Introduction

Molybdenum disulfide (MoS<sub>2</sub>) is a transition metal dichalcogenide with a layered structure where each layer consists of molybdenum atoms sandwiched between sulfur atoms. Three main applications of the material are in catalysis, opto-electronics, and tribology. The chemically active edges of MoS<sub>2</sub> nanoparticles have been used to catalyze various reactions, including, hydrogen evolution,<sup>1</sup> hydrotreatment of oil,<sup>2</sup> and pollutant removal.<sup>3,4</sup> In 2D form, MoS<sub>2</sub> is widely used as a catalyst for hydrogen evolution reactions<sup>5-7</sup> and CO<sub>2</sub> reduction.<sup>8-11</sup> In opto-electronics, single-layer MoS<sub>2</sub> is a semiconductor with a direct band gap that can be used to construct high efficiency transistors.<sup>12,13</sup> MoS<sub>2</sub> can be synthesized by chemical vapor

deposition to form large-area monolayers for use as atomically thin optical and photovoltaic devices.<sup>14</sup> In tribology, the weak van der Waals forces between layers provide low shear resistance, making MoS<sub>2</sub> an effective low-friction solid lubricant or, in nanoparticle form, a liquid lubricant additive.<sup>15–18</sup>

MoS<sub>2</sub> can be doped to enhance its properties.<sup>15</sup> Many different elements have been explored as possible MoS<sub>2</sub> dopants, particularly transition metals.<sup>15,19,20</sup> Dopants can provide various benefits, including altering the band gap,<sup>21</sup> catalytic reactivity,<sup>22</sup> hardness,<sup>23</sup> and nanoscale friction.<sup>24</sup> Here, we focus on Ni dopants, which have been shown to improve the performance of MoS<sub>2</sub> for various applications.<sup>2,25,26</sup> DFT simulations have found four metastable sites for a Ni dopant atom in the 2H-MoS<sub>2</sub> crystallographic structure.<sup>27</sup> Dopants can replace an Mo or an S atom in the crystal structure, or they can be intercalated between MoS<sub>2</sub> layers, either between a sulfur site in one layer and a molybdenum site in the other layer (tetrahedral with 4 Ni–S bonds), or between hexagonal holes in both layers (octahedral with 6 Ni–S bonds).<sup>28</sup>

Studies have investigated the atomistic structure of Ni-doped MoS<sub>2</sub> as well as its electronic and tribological properties. In doped MoS<sub>2</sub> nano-clusters, the Ni dopant was reported to substitute Mo atoms at edge sites leading to truncation of the cluster morphology relative to un-doped MoS<sub>2</sub>.<sup>19</sup> Conversely, Ni doping has also been found to enhance MoS<sub>2</sub> crystal size by increasing the mobility of edge planes during crystallization.<sup>29</sup> It has been observed that Ni doping can also transform the 2H-MoS<sub>2</sub> structure to the metallic 1T phase.<sup>30,31</sup>

Studies have shown that Ni doping increases the number of active sites which, in turn, improves the catalytic performance of MoS<sub>2</sub> in reduction of graphene oxide,<sup>32</sup> gas sensing,<sup>20</sup> and hydrogen evolution and production.<sup>25,33–35</sup> Ni also increases the S-vacancy defect density,<sup>36</sup> resulting in better catalytic activity for hydrogen evolution reaction.<sup>37</sup> Ni doping changes the electronic properties of MoS<sub>2</sub>:<sup>37–39</sup> specifically, doping enhances the low electrical conductivity of MoS<sub>2</sub>, making this material a promising candidate for electronic applications such as batteries.<sup>40,41</sup> In tribology, it has been shown that MoS<sub>2</sub> films co-sputtered with Ni

compare favorably to un-doped MoS<sub>2</sub> in terms of friction, wear, and useful life of mechanical parts.<sup>23,42–44</sup> The improvement in the tribological performance of MoS<sub>2</sub> is particularly notable at low temperatures, which makes Ni-doped MoS<sub>2</sub> ideal as a solid lubricant for space applications where performance at extreme conditions is critical.<sup>45,46</sup>

Ni-doped MoS<sub>2</sub> has been studied using *ab initio* density functional theory (DFT) calculations. Such calculations have shown that the activity of edge sites is doubled<sup>47</sup> and that gas adsorption and sensing is enhanced<sup>48,49</sup> by Ni. Other studies showed that Ni doping improves the catalytic performance of MoS<sub>2</sub> by decreasing the surface sulfur-metal bonding energy,<sup>50</sup> as well as weakening the S–H bond strength.<sup>51</sup> Previous DFT-based studies have provided information about structures, thermodynamics, vibrational properties, elasticity, and inter-layer binding in Ni-doped bulk 2H, bulk 3R, and monolayer 1H-MoS<sub>2</sub>.<sup>27,28</sup> DFT studies have also examined the energies and structural changes in frictional sliding of Ni-doped 2H and bilayer MoS<sub>2</sub>,<sup>52</sup> and the range of different reconstructed phases accessible by Ni-doping of monolayer 1T-MoS<sub>2</sub>.<sup>53</sup> However, such calculations are computationally demanding, limiting the time- and size-scales of model systems that can be studied.

An alternative simulation approach is molecular dynamics (MD) based on empirical models, or force fields, that describe the interactions between atoms. Several force fields have been developed, or optimized, for MoS<sub>2</sub>. First, a Stillinger-Weber force field was developed for MoS<sub>2</sub> and used to calculate mechanical and thermal properties of single layer MoS<sub>2</sub>.<sup>54,55</sup> However, the force field could not capture the behavior of MoS<sub>2</sub> at states far from equilibrium,<sup>56</sup> and did not include parameters for interlayer interactions. A custom, interpretable force field compatible with various non-reactive potential formalisms was developed for 2H-MoS<sub>2</sub><sup>57</sup> as well as for Cr-doped 2H-MoS<sub>2</sub>.<sup>58</sup> Despite accurate representation of energetic, mechanical, and surface properties, these potentials do not model the formation and breaking of chemical bonds. A many-body Mo/S potential based on the Reactive Empirical Bond Order (REBO) and Tersoff potentials was developed for MoS<sub>2</sub>.<sup>59</sup> The force field was able to reproduce expected lattice constants as well as mechanical properties of MoS<sub>2</sub>, but it was

unable to accurately model surface energy.

Several force fields within the ReaxFF formalism, that captures the formation and breaking of chemical bonds, have been parameterized for MoS<sub>2</sub> as well.<sup>56,60-62</sup> These force fields have been used in simulations of crystallization,<sup>56,60-63</sup> active edge sites,<sup>64</sup> creation of vacancies,<sup>56,65,66</sup> distribution and dynamics of defects,<sup>67</sup> mechanical properties of MoS<sub>2</sub> monolayer heterostructures,<sup>68-70</sup> and tribological behavior of multi-layer MoS<sub>2</sub>.<sup>71</sup> However, to investigate Ni-doped MoS<sub>2</sub>, force field parameters that include the interactions between Ni and MoS<sub>2</sub> are needed, which is a challenge as new interactions are introduced and the dopant's effect on the otherwise weak interlayer interactions must be described.

In this study, two new ReaxFF force fields were developed for Ni-doped MoS<sub>2</sub>. The force field parameters were optimized by comparing ReaxFF energies to those obtained from a large set of DFT calculations of the equation of state of Ni-doped 2H-MoS<sub>2</sub> under uniaxial, biaxial, triaxial, and in-plane shear strain. DFT calculations were performed with Ni dopants at each of four different sites: Mo-substituted, S-substituted, octahedral, and tetrahedral intercalation. The resulting ReaxFF force field was evaluated based on relaxed bond lengths and structural parameters in 2H, and as well as calculations of structures not in the training set such as doped 1H and 1T monolayers and doped 2H with vacancies as well as sliding. Finally, we demonstrated the use of the new force field to the study of sputter deposition and annealing of Ni-doped MoS<sub>2</sub>, pointing the way to future applications.

## Methods

### DFT Calculations

As in our previous work on thermodynamics and vibrational properties of Ni-doped MoS<sub>2</sub>,<sup>27</sup> the plane-wave density functional theory (DFT) code Quantum ESPRESSO<sup>72</sup> was used for quantum calculations. The Perdew-Burke-Ernzerhof<sup>73</sup> (PBE) generalized gradient approximation was used with Grimme-D2<sup>74</sup> van der Waals correction, and the electron-ion

interaction was described with optimized norm-conserving Vanderbilt pseudopotentials<sup>75</sup> parametrized by Schlipf and Gygi.<sup>76</sup> All DFT computations used a kinetic energy cutoff of 60 Ry. PBE + Grimme-D2 has been shown to accurately describe the lattice parameters, elastic constants, and phonon frequencies of MoS<sub>2</sub>.<sup>27</sup>

The training set was composed of 2H-MoS<sub>2</sub> in  $2 \times 2 \times 1$  supercells, where the third direction is perpendicular to the basal plane of the layers. Pristine 2H-bulk structures have six atoms per unit cell; a half-shifted Monkhorst-Pack  $k$ -grid of  $4 \times 4 \times 4$  was used. Atomic coordinates were relaxed using force thresholds of  $10^{-4}$  Ry/Bohr and the stresses were relaxed to 0.1 kbar. The relaxed lattice parameters of the hexagonal cell are  $a = b = 3.19 \text{ \AA}$ ,  $c = 12.40 \text{ \AA}$ ,  $\alpha = \beta = 90^\circ$ , and  $\gamma = 120^\circ$ . The dopant sites were chosen because they are stable or meta-stable;<sup>27</sup> other sites such as intralayer interstitial or S-S bridge intercalation would relax to other structures. The stable doped structures (Mo-substituted, S-substituted, and intercalation at the tetrahedral and octahedral sites, shown in Figure 1) were taken from Guerrero et al.<sup>27</sup>, constructed with one Ni atom in each  $2 \times 2 \times 1$  supercell. For validation, defect calculations in  $3 \times 3 \times 1$  supercells used a  $3 \times 3 \times 4$   $k$ -grid. The training set systems are shown in Figure 1. For convenience in reactive MD calculations, the results were used to construct nearly orthorhombic ( $\alpha = \beta = 90^\circ$ ) conventional cells with twice the number of atoms and twice the energy.

Strained 2H-bulk structures were studied under six strain conditions: uniaxial  $x$ -strain, uniaxial  $z$ -strain, biaxial  $xy$ -strain, triaxial strain, and  $xy$ -shear. Note that due to exact symmetries in the pristine structure, and approximate symmetries in the doped structures,<sup>27</sup> uniaxial  $y$ -strain would not provide further distinct information. For each strain direction, seven points were sampled with large strains ranging from -15% to 15% in intervals of 5%. Similarly, shear calculations were performed for seven points with shearing angles (the angle between orthogonal  $a$  and  $b$  lattice vectors as shown in the inset of Figure 6b) between  $\sim 72^\circ$  and  $108^\circ$ . In each case, the atomic forces were relaxed to  $10^{-4}$  Ry/Bohr with fixed lattice vectors.

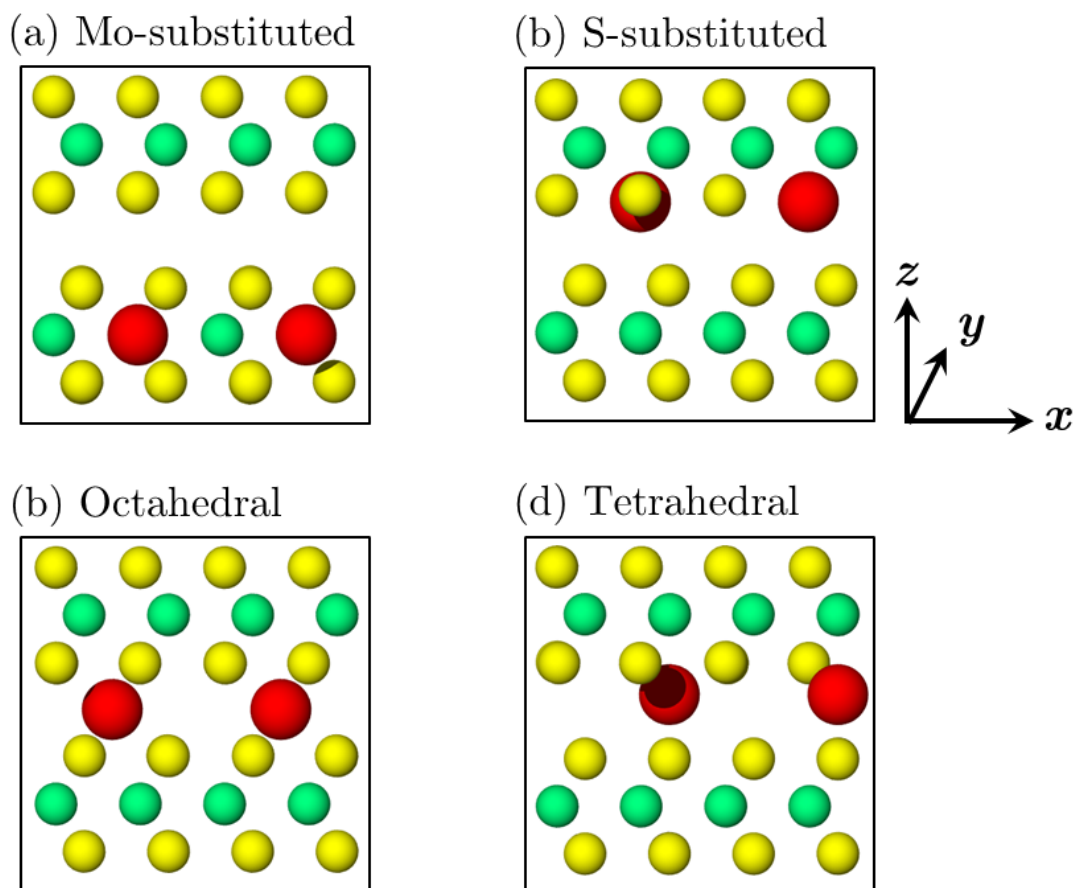


Figure 1: Side views of the training set structures, illustrating the four possible locations of the Ni dopant within MoS<sub>2</sub>: (a) Mo-substituted, (b) S-substituted, (c) octahedral intercalation, and (d) tetrahedral intercalation. Sphere colors indicate S (yellow), Mo (green), and Ni (red).

## ReaxFF Force Field and Parameterization

ReaxFF is a reactive empirical force field based on bond order and bond distance that originally was developed for hydrocarbons.<sup>77</sup> Over the years, many different parameters have been developed for various chemical systems. ReaxFF accounts for the contributions of various partial energy terms that enable ReaxFF to accurately model covalent and ionic bonds as well as non-bonded interactions. The total energy in the force field is the sum of the bond energy, over-coordination and under-coordination energy corrections, angle strain, torsion energy, torsion conjugation, van der Waals, and Coulomb energies. A detailed explanation

of all terms can be found in the original ReaxFF article.<sup>77</sup>

We started from two different parameter sets that were previously developed for S/Mo interactions, one reported in 2017<sup>56</sup> and the other reported in 2022.<sup>62</sup> The 2017 potential was developed specifically for single-layer MoS<sub>2</sub>, with a focus on its mechanical response with and without vacancies, and included parameters to model interactions between MoS<sub>2</sub> and oxygen. Then, the 2022 potential was developed by modifying the Mo/S parameters in the 2017 potential to better capture crystallization of MoS<sub>2</sub> in bilayer and bulk form. We introduced Ni parameters for both the 2017 and the 2022 force fields, starting with Ni/Mo<sup>78</sup> and Ni/S<sup>79</sup> parameters reported in previous studies. Since this study uses bulk DFT training data, and has an application focus on deposition of crystalline MoS<sub>2</sub>, we report the results for the new potential based on the 2022 parameters in the main text. However, results for the potential based on the 2017 force field as well as both potential files are available as supporting information.

Our force field was trained against the DFT data by optimizing the parameters specifically for Mo-S-Ni, S-Mo-Ni, and S-Ni-Mo valence angles. Other parameters, such as those for Ni-S and Mo-Ni bonds, remained fixed to literature values. The bond angle parameters were the equilibrium angle, first and second force constants, undercoordination parameter, and energy/bond order. The process of parameterization included calculating the potential energy of each structure ( $E^{\text{ReaxFF}}$ ) which was then compared to the energy obtained from DFT for the same structure ( $E^{\text{DFT}}$ ). A weighted error was calculated as:

$$\text{Error} = \sum_i \left( \frac{E_i^{\text{ReaxFF}} - E_i^{\text{DFT}}}{w_i} \right)^2 \quad (1)$$

where  $w_i$  is the weight associated with each data point on the energy plots. The weights were chosen to prioritize minimizing the difference between the DFT and the ReaxFF energies for near-equilibrium structures. The parameters were optimized by the single-parameter search optimization technique<sup>80</sup> in the stand-alone ReaxFF package. The energy difference between each strained and equilibrated structure as obtained from ReaxFF and DFT was plotted as



a function of strain for each strain direction. The same was done for sheared structures at each shearing angle. The parameterization process was repeated until the shapes of the energy plots were as similar as possible between ReaxFF and DFT. This procedure has been used previously to optimize ReaxFF parameters for various chemical systems.<sup>56,62,81–84</sup> The developed force field was evaluated and then demonstrated using energy minimization and dynamics simulations with the Large-scale Atomic/Molecular Massively Parallel Simulator (LAMMPS) code.<sup>85</sup>

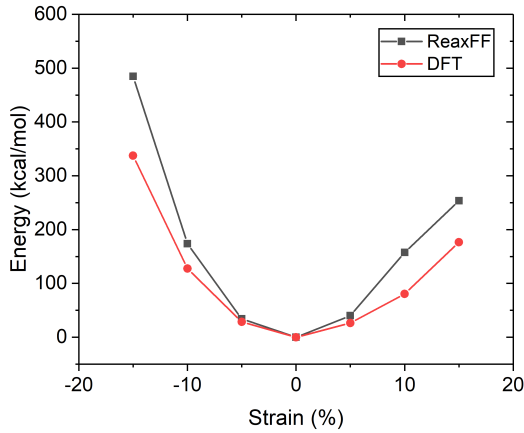
## Results and Discussion

### Force Field Parameterization

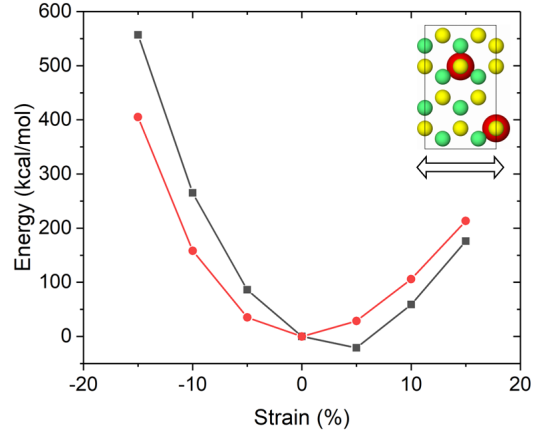
The energies of all four structures under all five strain conditions were used in the training of the ReaxFF force field. The results for uniaxial straining in the  $x$ - and  $z$ -directions of the four Ni-doped MoS<sub>2</sub> structures are shown in Figure 2 and Figure 3, respectively. The equation of state energies given are those of the conventional cell, with respect to the energy in each method of the unstrained structure. The structures used in ReaxFF result from a relaxation with fixed cell parameters, starting from the DFT structures.

We can begin by examining the energy difference between unstrained octahedrally and tetrahedrally intercalated structures. While Mo-substituted, S-substituted, and intercalated structures have different stoichiometries and cannot be compared in energy without assumptions about the chemical potential,<sup>27</sup> we can directly compare the energies of the two intercalated structures. In DFT, tetrahedral is lower in energy by 39.1 kcal/mol in these structure (0.841 eV per Ni atom).<sup>27</sup> We find a very close level of agreement in ReaxFF, which gives tetrahedral lower in energy by 41.0 kcal/mol. This agreement is essential for the correct structures to appear in MD simulations, and also demonstrates the ability of our ReaxFF parametrization to describe accurately the energy difference between the 6-bonded octahedral and 4-bond tetrahedral environment.

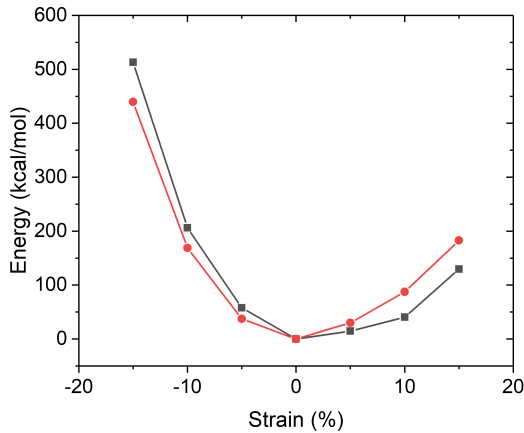
The uniaxial ReaxFF energies are in reasonably good agreement with the DFT energies, despite the large strains that were applied. Discrepancies are largest at large strain. Shapes are similar, though for  $x$  strain and S-substituted, ReaxFF actually has a minimum shifted to +5% strain (vs the DFT structure), and for  $z$  strain and Mo-substituted the minimum is shifted to -5%. For  $x$  strain, Mo-substituted has larger energy value in ReaxFF than in DFT for all strains, whereas in the other cases, ReaxFF is higher for compressive strains and lower for tensile strains. For  $z$  strain, the ReaxFF energies are larger than in DFT in general, showing an overestimation of the elastic modulus in the  $z$  direction. If we compare the level of discrepancy between ReaxFF and DFT here to the results of uniaxial strain for pristine MoS<sub>2</sub> in the 2017 parametrization (Fig. S3 in Ref.<sup>56</sup>), we find the discrepancy is similar for the intercalated structures, but larger for substituted structures.



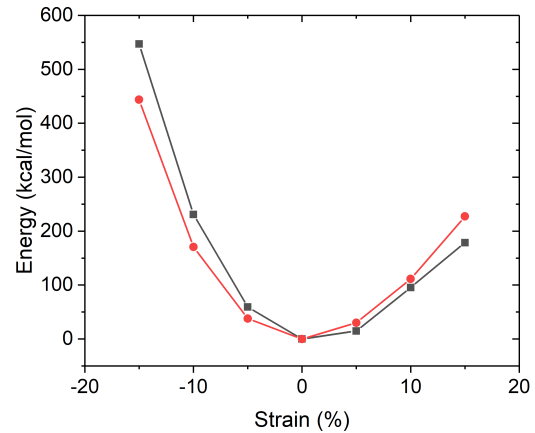
(a) Mo-substituted



(b) S-substituted



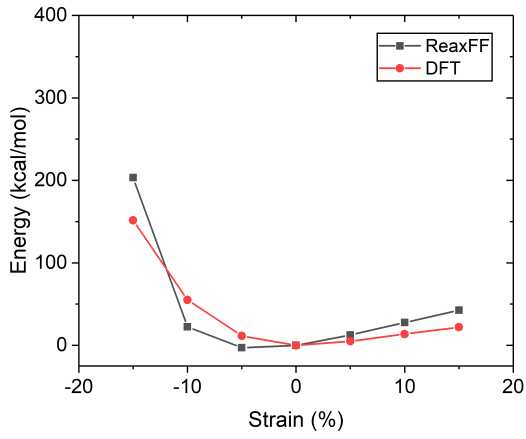
(c) Octahedral



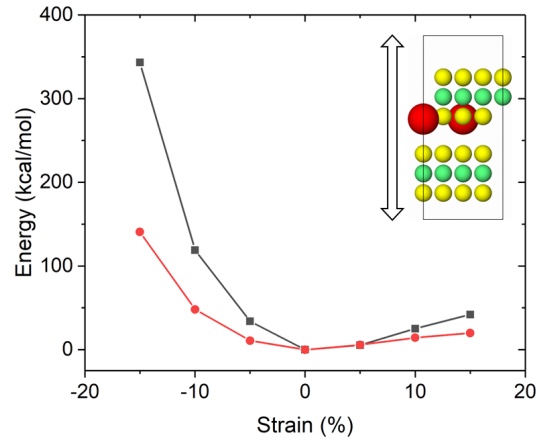
(d) Tetrahedral

Figure 2: Equations of state calculated from DFT (red) and ReaxFF (black) for the Ni-doped  $\text{MoS}_2$  structures strained uniaxially in the  $x$ -direction. The inset in (b) shows a top view of the S-substituted structure with an arrow indicating the strain direction.

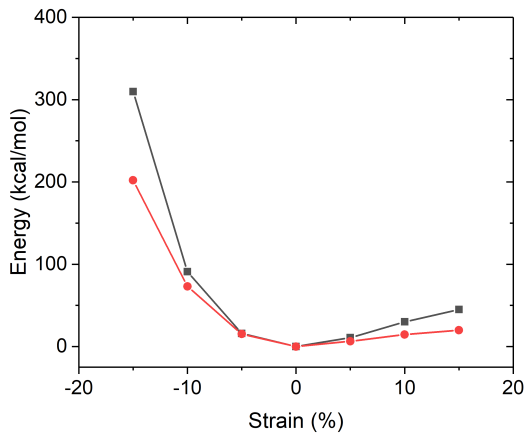
The results for biaxial and triaxial straining (where the specified strain value is applied to each axis) are shown in Figure 4 and 5, respectively, providing significantly better ReaxFF/DFT agreement than the uniaxial strain. We attribute the better agreement to the fact that bond angles change less in biaxial or triaxial strain than in uniaxial strain, so there is less dependence on the newly parametrized bond-angle terms in this work, and more dependence on the well-fit parameters we have taken from the literature. The energies as obtained from DFT calculations for the highest strains are  $\sim 1000$  kcal/mol for biaxial



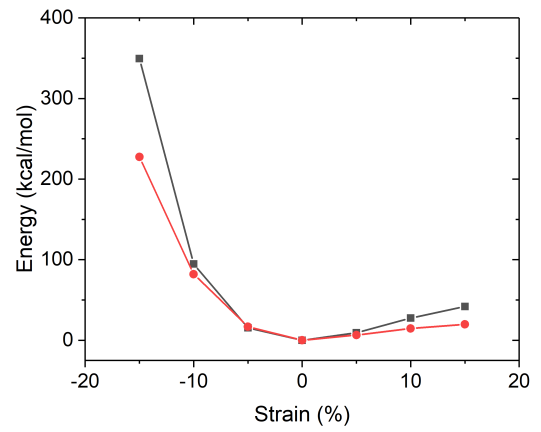
(a) Mo-substituted



(b) S-substituted



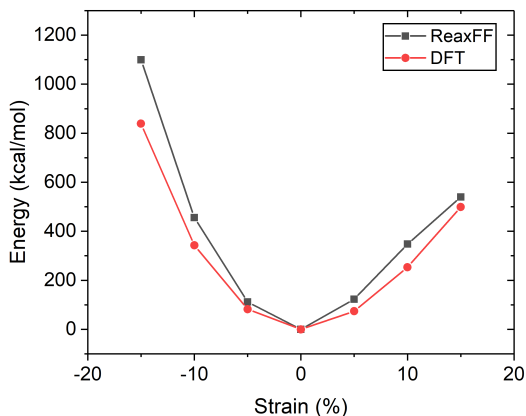
(c) Octahedral



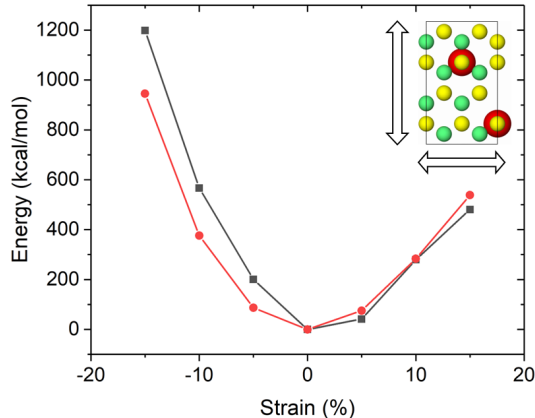
(d) Tetrahedral

Figure 3: Equations of state calculated from DFT (red) and ReaxFF (black) for the Ni-doped  $\text{MoS}_2$  structures strained uniaxially in the  $z$ -direction. The inset in (b) shows a side view of the S-substituted structure with an arrow indicating the strain direction.

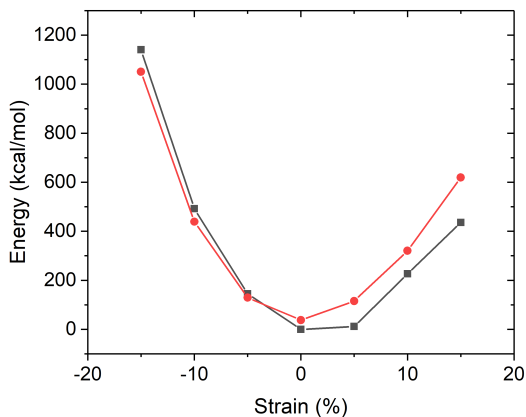
strain and even higher (up to  $\sim 1800$  kcal/mol) in the case of triaxial strain. Nevertheless, our force field is in excellent agreement with the DFT for the case of biaxial as well as triaxial straining. The ReaxFF energies are consistent with DFT for both the near-equilibrium structures and the far-from-equilibrium energies, and provide the correct minimum energy at zero strain.



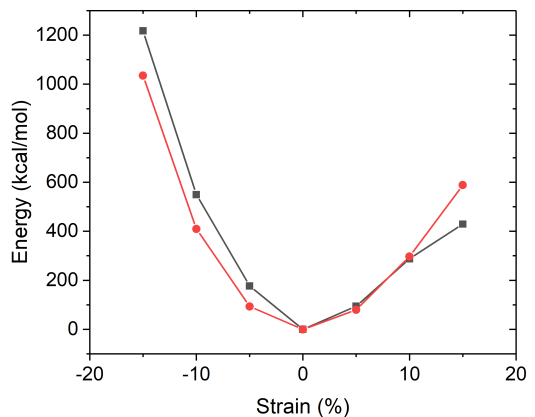
(a) Mo-substituted



(b) S-substituted



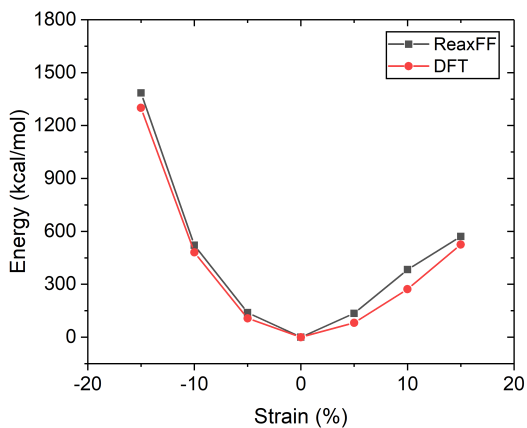
(c) Octahedral



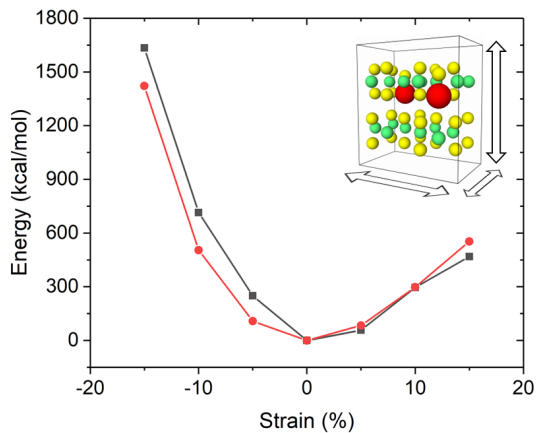
(d) Tetrahedral

Figure 4: Equations of state as obtained from DFT (red) and ReaxFF (black) for the Ni-doped  $\text{MoS}_2$  structures strained biaxially for Mo-substituted, S-substituted, octahedral, and tetrahedral positions. The inset in (b) shows a top view of the S-substituted structure with two arrows indicating the strain directions.

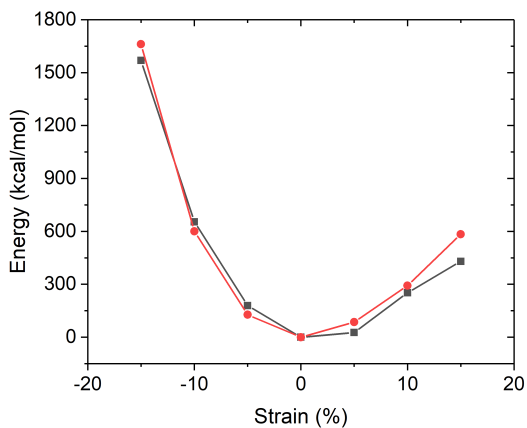
Finally, the ReaxFF energies for sheared structures were compared with DFT. Figure 6 shows excellent agreement for near-equilibrium as well as far-from-equilibrium structures.



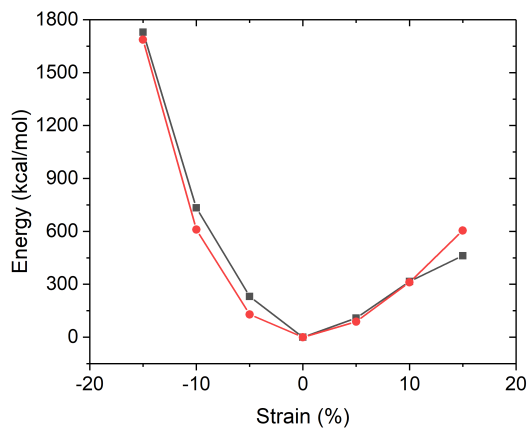
(a) Mo-substituted



(b) S-substituted



(c) Octahedral



(d) Tetrahedral

Figure 5: Equations of state as obtained from DFT (red) and ReaxFF (black) for the Ni-doped  $\text{MoS}_2$  structures strained triaxially for Mo-substituted, S-substituted, octahedral, and tetrahedral positions. The inset in (b) shows a perspective view of the S-substituted structure with three arrows indicating the strain directions.

The minimum is correctly at  $90^\circ$  and the shape is close and correctly symmetrical. Mo-substituted has an overestimated shear modulus whereas S-substituted is very close, and octahedral and tetrahedral intercalation have an underestimated shear modulus.

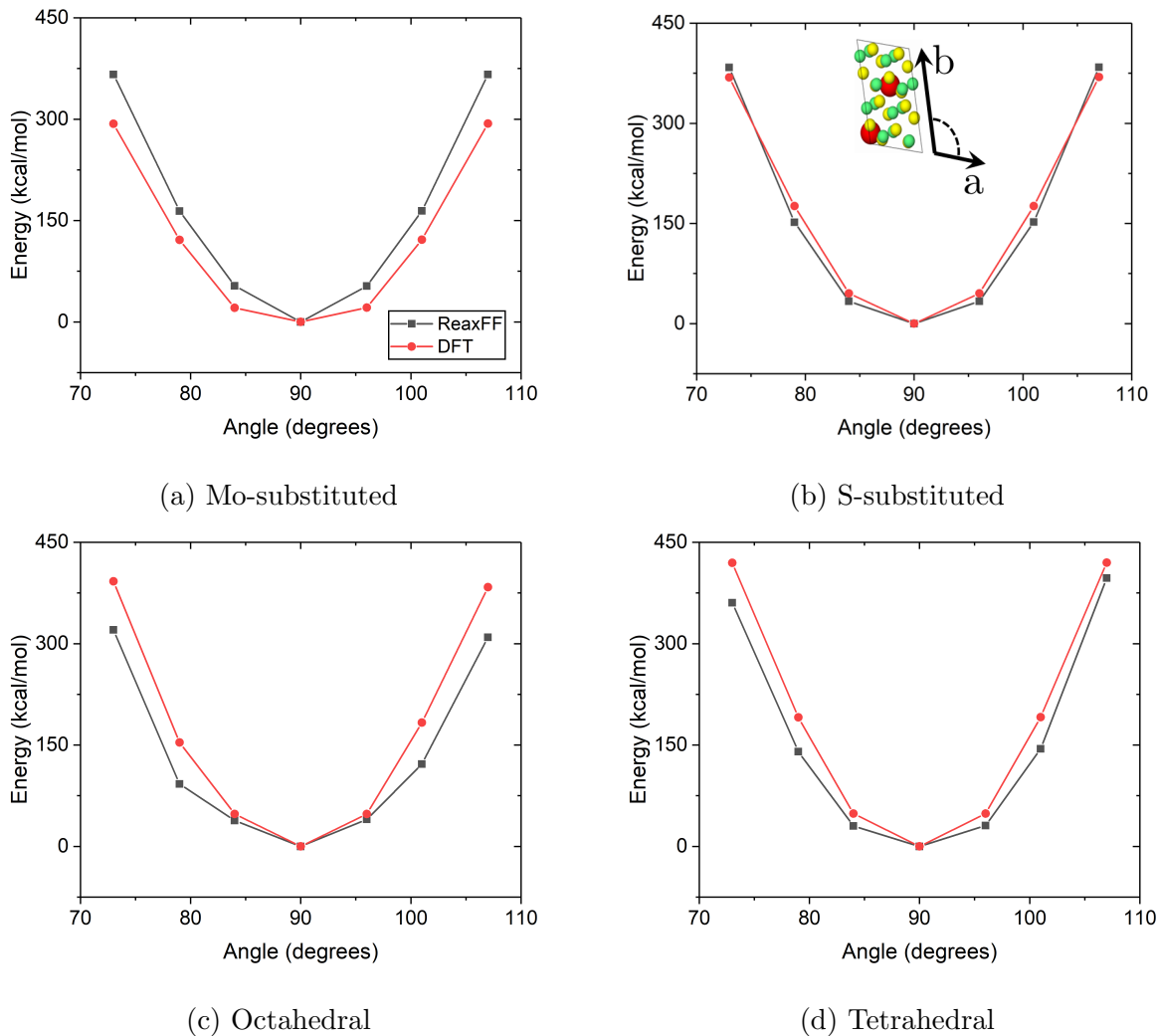


Figure 6: ReaxFF (black) and DFT (red) energies obtained for Ni-doped  $\text{MoS}_2$  structures sheared in the  $xy$  basal plane for (a) Mo-substituted, (b) S-substituted, (c) octahedral, and (d) tetrahedral structures. The inset in (b) shows a top view of the basal plane of the S-substituted structure with arrows indicating the shearing angle as calculated from the angle between in-plane conventional cell vectors  $a$  and  $b$ .

## Force Field Evaluation

Next we evaluated the force field’s ability to predict parameters that were not included in the training. This evaluation was based on atom positions and distances obtained from relaxation of the model structures using energy minimization with the conjugate gradient algorithm with force and energy criteria of  $10^{-6}$  kcal/mol-Å and  $10^{-6}$  (unitless), respectively, and a simulation of periodic cell optimization with a target zero stress tensor. First, the Ni–Mo and Ni–S atomic distances in all four structures were calculated. Results for Ni–Mo and Ni–S bond lengths are shown in Table 1a and 1b, respectively.

**Table 1: Atomic distances (below 3.6 Å) between Ni and its neighbors from DFT and ReaxFF. Repeated distances are indicated with a multiplier.**

Structure	DFT (Å)	ReaxFF (Å)
Mo-substituted	$3.20 \times 6$	$3.19 \times 6$
S-substituted	$2.55 \times 3$	$2.76 \times 3$
Octahedral	$3.57 \times 6$	3.30/3.44/3.47–4.36/4.38/4.50
Tetrahedral	$2.61 \times 1$	$2.85 \times 1$

**(a) Ni–Mo distances**

Structure	DFT (Å)	ReaxFF (Å)
Mo-substituted	$2.38 \times 3$	$2.36 \times 3$
S-substituted	$3.18 \times 6$	$3.25 \times 6$
Octahedral	$2.34 \times 3, 2.38 \times 3$	2.24/2.24/2.37–2.83/3.04/3.09
Tetrahedral	$2.17 \times 3, 2.12 \times 1$	$2.32 \times 3, 2.27 \times 1$

**(b) Ni–S distances**

In most cases, the differences between ReaxFF and DFT bond lengths were within 0.1 Å, indicating the force field can accurately capture bond lengths within the Ni-doped MoS<sub>2</sub> structure. The same analysis for Mo–S bond lengths revealed that the difference between the DFT and ReaxFF calculated values was less than 0.1 Å for most cases and less than 0.2 Å for some cases in the octahedral and tetrahedral intercalation structures. For the pristine structure, the Mo–S bond length difference between DFT and ReaxFF calculated using the original 2022 parameters was 0.04Å. Generally, for Ni-doped MoS<sub>2</sub>, ReaxFF predicted



a slightly larger interlayer separation resulting an increase in the bond distances. The local symmetry around Ni, as shown by the multiplicity of the atomic distances, was correctly preserved in every case except the octahedral intercalation. However, for octahedral intercalation, the larger separation of the two MoS<sub>2</sub> layers in ReaxFF resulted in breaking of the symmetry that was predicted by DFT calculations, and much larger deviations in bond lengths.

Next, the force field’s ability to reproduce Ni-doped MoS<sub>2</sub> structures with correct lattice parameters was tested. The parameters considered, illustrated in Figure 7, were the conventional cell vectors,  $a$  and  $b$ , the average distance  $h$  between S planes in a single layer, and the average interlayer separation  $d$ . The values for these parameters after structure relaxation in DFT and in ReaxFF are shown in Table 2. The difference between the DFT- and ReaxFF-calculated parameters was less than 0.1 Å for most doped structures, as well as the pristine MoS<sub>2</sub> case which is shown for reference and relies only on the pre-existing Mo-S potential. This is consistent with the equation of state findings, since the optimized values of  $a$  and  $c = 2h + 2d$  are the minima of the uniaxial  $x$  and  $z$  curves. The most notable discrepancy is for  $d$  in the octahedral case, where ReaxFF overestimates by  $\sim 0.4$  Å.

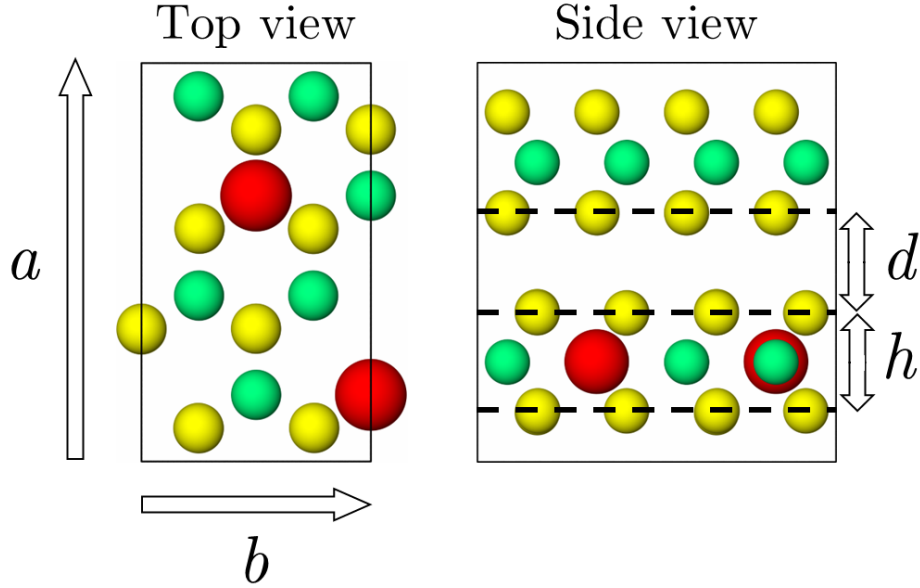


Figure 7: Structural parameters for Ni-doped  $\text{MoS}_2$  illustrated for Mo-substituted configuration: in-plane lattice constant  $a$ , average distance  $h$  between S planes in a single layer, and average interlayer separation  $d$ .

**Table 2: Comparison of structural parameters as obtained from DFT and ReaxFF for bulk Ni-doped  $\text{MoS}_2$**

Structure	$a$ (Å)		$b$ (Å)		$d$ (Å)		$h$ (Å)	
	DFT	ReaxFF	DFT	ReaxFF	DFT	ReaxFF	DFT	ReaxFF
Pristine	6.38	6.40	11.04	11.10	3.08	3.03	3.12	3.21
Mo-substituted	6.40	6.40	11.08	11.08	3.07	3.00	3.07	3.16
S-substituted	6.35	6.47	11.00	11.21	2.87	2.77	3.15	3.30
Octahedral	6.38	6.45	11.06	11.20	2.66	3.03	3.12	3.17
Tetrahedral	6.39	6.43	11.07	11.16	2.88	2.95	3.06	3.14

The accuracy of the developed force field was also tested in distinguishing the relative energies of Ni-doped 1H and 1T monolayer structures. We used  $2 \times 2$ ,  $3 \times 3$ , and  $4 \times 4$  in-plane supercells of the three-atom unit cell of 1H and 1T, where each supercell contained one Ni atom; these structures were then doubled to create orthogonal unit cells with two Ni atoms per cell. The different doping sites<sup>28,53</sup> were: adatoms at the hollow position (three-fold

hollow space between top S atoms), Mo atop (on top of Mo), or S atop (on top of S); Mo-substituted, or S-substituted. The pristine structures were also included for reference, which had been studied in the 2017 work.<sup>56</sup> Note that neither 1H or 1T structures nor adatoms were in our training data. Snapshots of representative structures (S atop) of different sizes (doping concentrations) are shown in Figure 8. The energy differences between 1H and 1T polytypes were compared between ReaxFF and DFT in Figure 8, using DFT results from Karkee et al.<sup>28</sup> and Karkee and Strubbe<sup>53</sup>. Results show that the force field can capture the energies corresponding to Ni adatoms with a small underestimation.

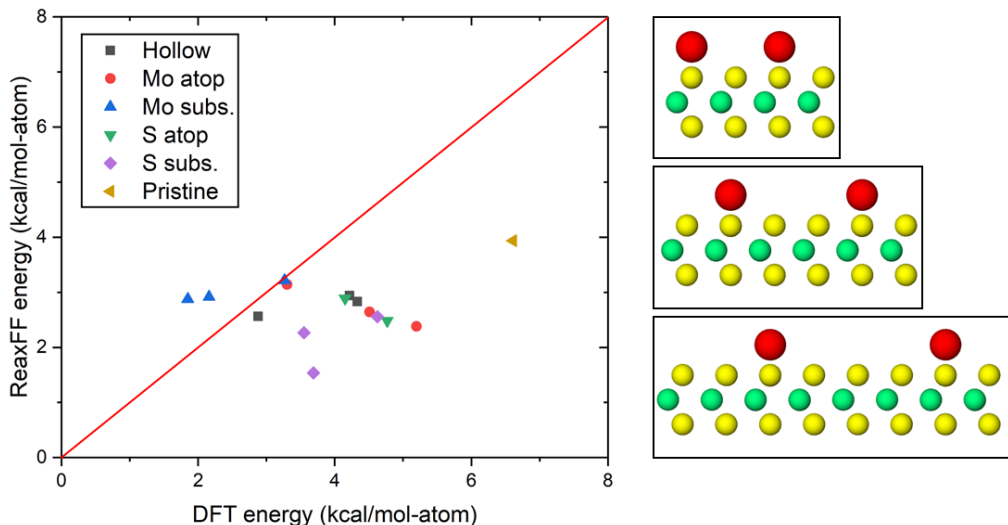


Figure 8: Energy difference between 1H and 1T polytypes for each structure of Ni-doped (or pristine)  $\text{MoS}_2$ . Results show energy differences of the right scale for ReaxFF, but with less variation. leading to underestimation by ReaxFF for some doping locations. Snapshots (right) show  $2 \times 2$ ,  $3 \times 3$ , and  $4 \times 4$  supercells of S atop site of 1H- $\text{MoS}_2$  (different size supercells correspond to different doping concentrations).

Given the prevalence of vacancies in real  $\text{MoS}_2$ <sup>86</sup> samples, and studies of vacancies with the 2017 ReaxFF potential,<sup>56</sup> we tested our reactive force field on defective bulk 2H structures that combine Mo or S vacancies and Ni dopants. In each case, the vacancy was located at the nearest Mo or S site to the Ni dopant. Structures based on a  $3 \times 3 \times 1$  supercell

were constructed and underwent variable-cell relaxation in DFT, and then the DFT-relaxed structure was converted to a conventional cell, imported to ReaxFF and relaxed using the developed force field. The goal to have an agreement between DFT and ReaxFF required that the final (i.e., after relaxation) atomic positions of Ni-doped MoS<sub>2</sub> atoms be the same (i.e., no structural changes during ReaxFF relaxation). A summary of atomic rearrangements during each relaxation is shown in Table 3.

**Table 3: Summary of atomic rearrangements of 2H-MoS<sub>2</sub> with a Ni dopant and a vacancy, both at variable locations. In intercalations and S-substituted with a vacancy, Ni moves into the vacancy. All rearrangements predicted by DFT remain in ReaxFF.**

Ni initial site	Vacancy initial site	Ni relaxed site	Vacancy relaxed site
Mo	Mo	Mo	Mo
Mo	S	Mo	S
S	Mo	Mo	S
S	S	S	S
Octahedral	Mo	Mo	-
Octahedral	S	S	-
Tetrahedral	Mo	Mo	-
Tetrahedral	S	S	-

Table 3 shows that, according to DFT, for the intercalated structures, Ni moved to the vacancy position, essentially converting an intercalated structure to a substituted structure (Mo-substituted for Ni filling an Mo vacancy and S-substituted for Ni filling an S vacancy). An example is shown in Fig. 9. This observation is consistent with the findings in Guerrero et al.<sup>27</sup> that the formation energy for tetrahedral intercalation in a  $3 \times 3 \times 1$  supercell is 0.401 eV, greater than the energy for filling an Mo vacancy with Ni (-2.575 eV), and for filling an S vacancy (0.194 eV). The formation energy for octahedral intercalation is 0.9 eV higher, making the migration to a vacancy yet more exothermic. The calculations performed here additionally show that these migrations have no barrier. We additionally observe that S-substituted Ni adjacent to an Mo vacancy moves to the Mo site, leaving behind an S

vacancy. The ReaxFF relaxed structures preserved the same rearrangements as in DFT for all combinations of dopant and vacancy positions.

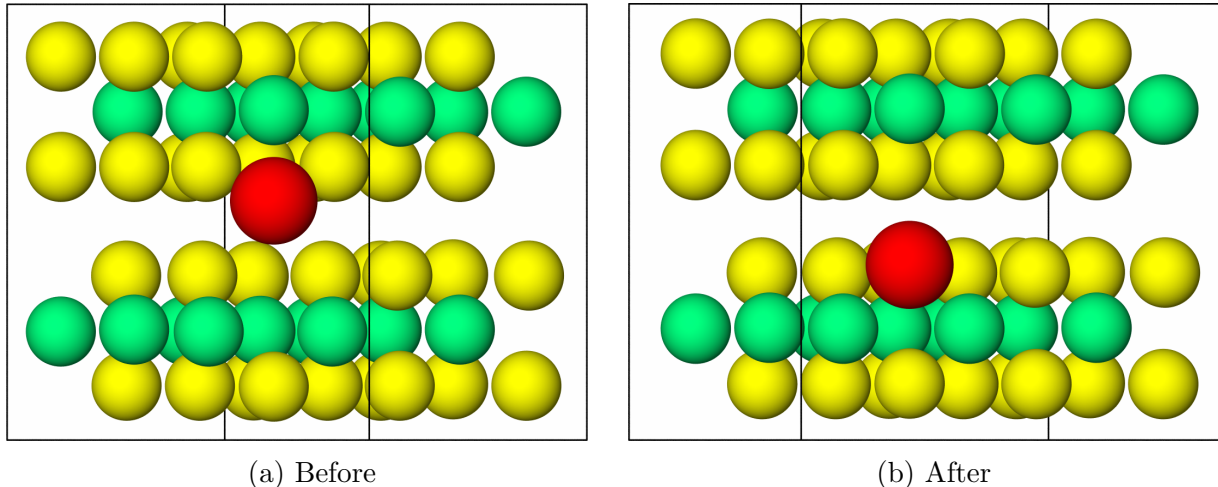


Figure 9: Relaxation of a dopant/vacancy structure as calculated by DFT: (a) tetrahedrally intercalated Ni adjacent to an S vacancy; (b) Ni has moved into the S site, forming S-substituted MoS<sub>2</sub>.

Lastly, we evaluated the potential in terms of its ability to model interlayer sliding. However, as shown in Figs. S6 and S7, the sliding energies from ReaxFF did not match those from DFT, except for the Mo-substituted case sliding in the  $x$ -direction. Even the original potential could not capture sliding energies in the  $y$ -direction (Fig. S8), since neither the original nor the doped potential was trained for sliding.

## Simulations of Deposition and Annealing

To demonstrate the newly developed force field, the process of sputter deposition and annealing to grow Ni-doped MoS<sub>2</sub> films<sup>87</sup> was simulated. The simulations were performed using LAMMPS in the NVT ensemble with the Langevin thermostat, a damping parameter of 10.0 fs, and a time step of 0.1 fs. The simulation box was  $2.5 \times 2.4 \times 10.0$  nm in the  $x$ -,  $y$ -, and  $z$ -directions, respectively, with periodic boundary conditions in the  $x$ - and  $y$ -directions. The initial configuration was a substrate consisting of bilayer 2H-MoS<sub>2</sub>, with the bottommost layer held fixed during the simulation.

Atoms were deposited from 7.0 nm above the substrate surface, and a reflective virtual wall (which reflects downward only) was placed parallel to the surface at a distance of 4.8 nm to ensure deposited atoms remain near the substrate. The deposition process followed a simulation protocol used previously for SiO<sub>2</sub> thin film formation.<sup>88</sup> First, energy minimization was performed to obtain the relaxed atomic positions, followed by thermal equilibration for 50 ps at room temperature. Next, Mo, S, and Ni atoms were continuously deposited onto the MoS<sub>2</sub> substrate at a 1:2 Mo to S ratio with Ni atoms replacing Mo atoms at 7% by weight, expected to promote Ni substitution for Mo.<sup>23</sup> The deposition rates for Mo and Ni were one atom every 40 fs with a deposition energy of 230 kcal/mol; for S atoms the deposition rate was one atoms every 20 fs with a deposition energy of 1.5 kcal/mol. Under typical experimental conditions, an inert gas such as argon is used to modulate the incident kinetics of the deposited Mo, S and Ni radicals. Following previous simulations of Si-O deposition,<sup>89</sup> a lower deposition energy was used to slow the sulfur atoms such that they act not only as radicals but as kinetic energy modulators, without the need to explicitly model argon. The total number of deposited S, Mo, and Ni atoms after 50 ps was 1000, 405, and 95, respectively. At the end of the deposition process, the system was equilibrated at 300 K for 50 ps.

The second stage was annealing the deposited Ni-doped MoS<sub>2</sub> film, following the simulation process used previously for the crystallization of un-doped MoS<sub>2</sub>.<sup>62</sup> The annealing process was carried out by heating the model at the end of the deposition stage to 5000 K over 50 ps at a ramping rate of 100 K/ps. The structure was equilibrated at high temperature for 50 ps. Then, the structure was cooled to 2000 K at a rate of 30 K/ps followed by equilibration for 300 ps to trigger nucleation. Finally, the model was cooled to 300 K over 170 ps (10 K/ps).

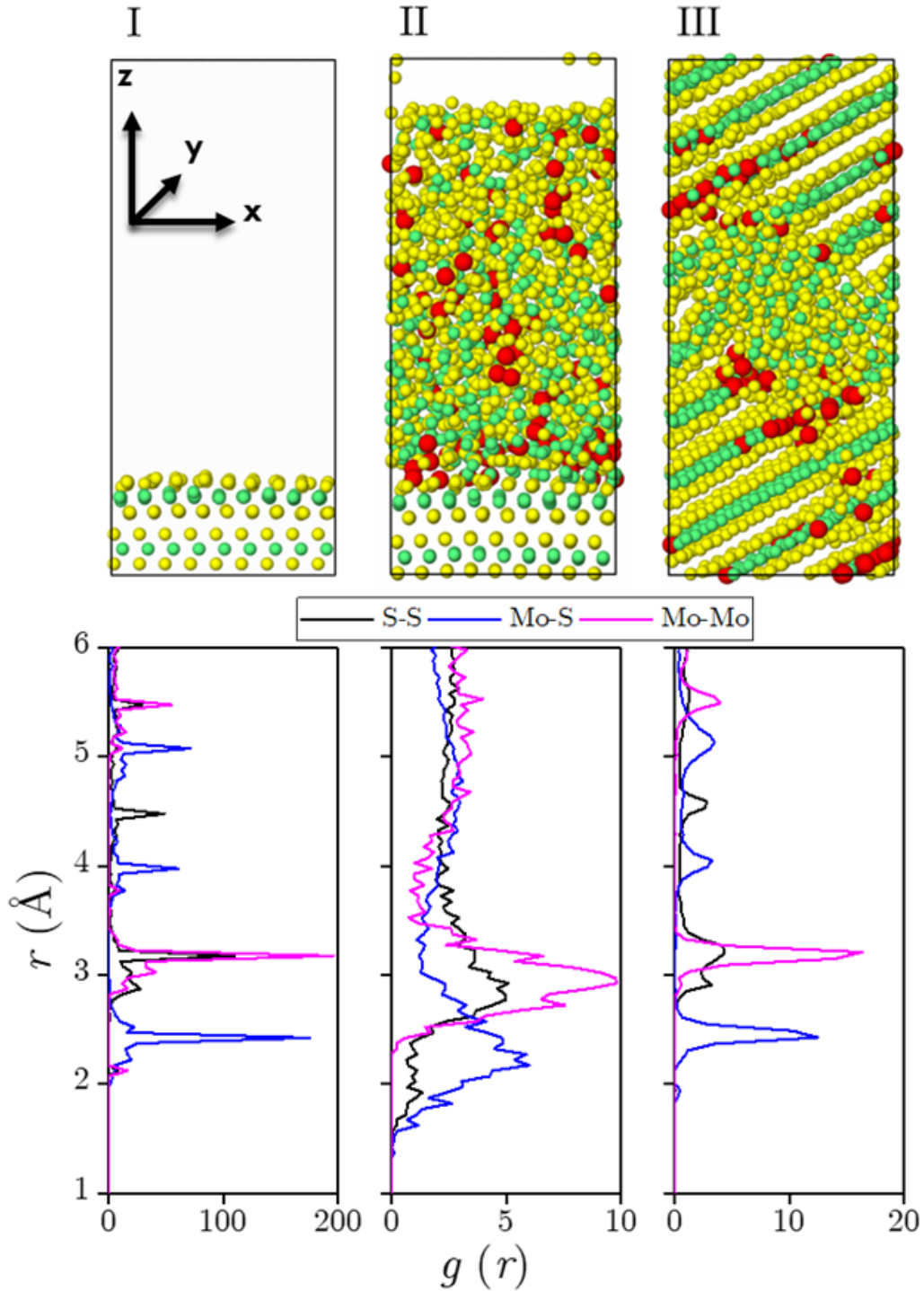


Figure 10: Side-view snapshots of the model system and radial distribution function (I) before deposition, (II) at the end of the deposition, and (III) at the end of the annealing stage. A clear transition from amorphous to crystalline is observed (II)  $\rightarrow$  (III). Spheres represent S (yellow), Mo (green), and Ni (red) atoms.

Snapshots of the model system before deposition, after deposition, and after annealing are shown in Figure 10(a), (b), and (c), respectively. Visually, the model system appears amorphous at the end of deposition, consistent with experimental observations for magnetron-sputtered MoS<sub>2</sub>,<sup>87,90</sup> but then is mostly crystalline after annealing, as observed after annealing in experiments.<sup>87,90</sup> Note that the middle region of the material (Figure 10(c)) does not appear crystalline from this view, but is in fact crystalline at an angle relative to the perspective shown here. An alternate angle from which the crystallinity of the entire model is visible is shown in Fig. S9. The crystallization process can be quantified using radial distribution functions (RDFs) of S–S, S–Mo, and Mo–Mo atom distances at the end of each stage of the simulation. The RDF of the initial crystal substrate after equilibration, shown in Figure 10(d), exhibits clear peaks indicative of a perfect crystal. At the end of the deposition, Figure 10(e) shows broad close-distance peaks and only weak further-distance (second neighbor) peaks, indicating an amorphous structure. Then, the RDF after annealing, shown in Figure 10(f), has the regular peaks again, only slightly broadened from the before-deposition peaks, confirming that the material is in fact crystalline.

Visual analysis of the simulation after annealing suggested that most of the Ni atoms positioned themselves at Mo sites, resulting in a Mo-substituted Ni-doped MoS<sub>2</sub> structure. To confirm this, the distribution of Ni–S and Ni–Mo distances at the end of annealing are shown in Figure 11(b). The heights of the first Ni–S (red) peaks after annealing are at similar distances to those observed in Figure 11(a) for the Mo–S (red) peak. We can conclude that Ni atoms are bonded to S more than to Mo, consistent with the Mo-substituted Ni-doped MoS<sub>2</sub> structure. Previous DFT calculations have shown that, under S-rich conditions, Mo-substituted is the most favorable doping location for Ni.<sup>27</sup> Visual analysis of the post-annealing simulations also indicated that the Ni atoms were not randomly distributed throughout the crystal, but rather formed few-atom clusters. This observation is consistent with phase separation predicted for Mo substitution according to convex hull analysis of DFT calculations.<sup>27</sup> Similar behavior has been previously observed for gold atoms co-sputtered



with MoS<sub>2</sub>,<sup>91</sup> which is further support for the physical realism of these simulations and the new force field.

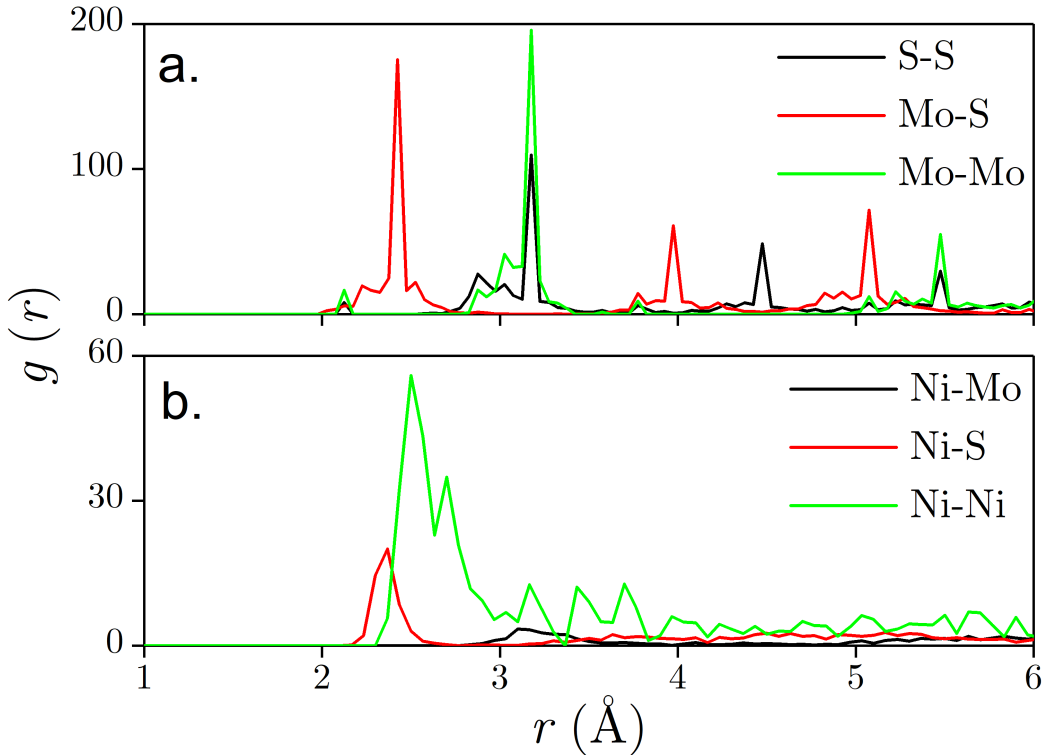


Figure 11: Radial distribution functions for (a) 2H MoS<sub>2</sub> substrate before deposition and (b) system after annealing. Similar peak locations for Ni-S and Mo-S, and for Ni-Mo and Mo-Mo, indicate occupation of Mo sites by Ni after annealing.

## Conclusion

Two new ReaxFF force fields were developed for Ni-doped MoS<sub>2</sub>. The force fields were developed by adding the parameters for Ni-Mo-S, Ni-S-Mo, and S-Ni-Mo angles to a previously optimized force field for MoS<sub>2</sub>,<sup>56,62</sup> and tuning those parameters to match DFT-calculated energies. The parameterization was based on strained DFT calculations of Mo-substituted, S-substituted, octahedral, and tetrahedral intercalation structures of the Ni dopant. Both force fields showed accurate and reliable results with the force field that was based on the 2022 parameters performing slightly better. Hence, the results from the 2022 parameters

were shown in the main text. However, since the two original parameter sets were optimized for different MoS<sub>2</sub> models, i.e., single-layer versus bulk, the 2017 parameters' equation of state results were included in the SI section. The final force field developed based on the 2022 potential was able to accurately predict the energy difference between tetrahedral and octahedral intercalation, lengths of Mo–Ni and S–Ni bonds, lattice constants, S–S distance, and interlayer separation. Furthermore, the developed force field agreed with DFT on the relaxed geometries of Ni-doped MoS<sub>2</sub> structures with vacancies. We note that the force field was not trained for interlayer sliding,<sup>52</sup> and our initial testing indicates that it was not able to accurately capture sliding behavior for most dopant configurations; improvement of the force field to capture sliding energies could be considered in future work. However, the force field is robust for modeling the crystal structures of Ni-doped MoS<sub>2</sub> and their elastic behavior, as well as the phase transition between amorphous and crystalline, and also the underlying mechanisms of doping. The ReaxFF force fields developed in this work will enable future simulation-based studies of the fundamental mechanisms by which Ni dopants affect MoS<sub>2</sub> for applications in catalysis and tribological, as well as other possible new applications of the material.

## Supporting Information Available

Comparison between ReaxFF and DFT energies obtained from the force field developed based on the 2017 ReaxFF MoS<sub>2</sub> parameters,<sup>56</sup> sliding potentials for doped and pristine MoS<sub>2</sub>, and alternate snapshot of the post-annealing doped material (PDF); relaxed structures from DFT (.POSCAR) and ReaxFF (.XYZ) and their minimized energies; and ReaxFF parameter files (.txt) developed based on the 2017<sup>56</sup> and 2022<sup>62</sup> MoS<sub>2</sub> parameters.

## Acknowledgments

We acknowledge Rijan Karkee for providing Ni-doped 1T and 1H structures. Computing resources were provided by the Multi-Environment Computer for Exploration and Discovery (MERCED) cluster at UC Merced, funded by National Science Foundation Grant No. ACI-1429783, and the National Energy Research Scientific Computing Center (NERSC), a U.S. Department of Energy Office of Science User Facility operated under Contract No. DE-AC02-05CH11231. This work was supported by the Merced nAnomaterials Center for Energy and Sensing (MACES), a NASA-funded research and education center, under awards NNX15AQ01 and NNH18ZHA008CMIROG6R, and by UC Merced start-up funds.

## References

- (1) Jaramillo, T. F.; Jørgensen, K. P.; Bonde, J.; Nielsen, J. H.; Horch, S.; Chorkendorff, I. Identification of active edge sites for electrochemical H<sub>2</sub> evolution from MoS<sub>2</sub> nanocatalysts. *Science* **2007**, *317*, 100–102.
- (2) Jeong, G.; Kim, C. H.; Hur, Y. G.; Han, G.-H.; Lee, S. H.; Lee, K.-Y. Ni-Doped MoS<sub>2</sub> Nanoparticles Prepared via Core–Shell Nanoclusters and Catalytic Activity for Upgrading Heavy Oil. *Energy Fuels* **2018**, *32*, 9263–9270.
- (3) Araki, Y.; Honna, K.; Shimada, H. Formation and catalytic properties of edge-bonded molybdenum sulfide catalysts on TiO<sub>2</sub>. *J. Catal.* **2002**, *207*, 361–370.
- (4) Bhattacharya, D.; Mukherjee, S.; Mitra, R. K.; Ray, S. K. Size-dependent optical properties of MoS<sub>2</sub> nanoparticles and their photo-catalytic applications. *Nanotechnology* **2020**, *31*, 145701.
- (5) Deng, J.; Li, H.; Xiao, J.; Tu, Y.; Deng, D.; Yang, H.; Tian, H.; Li, J.; Ren, P.; Bao, X. Triggering the electrocatalytic hydrogen evolution activity of the inert two-dimensional MoS<sub>2</sub> surface *via* single-atom metal doping. *Energy Environ. Sci.* **2015**, *8*, 1594–1601.

- (6) Zong, X.; Na, Y.; Wen, F.; Ma, G.; Yang, J.; Wang, D.; Ma, Y.; Wang, M.; Sun, L.; Li, C. Visible light driven H<sub>2</sub> production in molecular systems employing colloidal MoS<sub>2</sub> nanoparticles as catalyst. *Chem. Commun.* **2009**, *30*, 4536–4538.
- (7) Cuddy, M. J.; Arkill, K. P.; Wang, Z. W.; Komsa, H. P.; Krasheninnikov, A. V.; Palmer, R. E. Fabrication and atomic structure of size-selected, layered MoS<sub>2</sub> clusters for catalysis. *Nanoscale* **2014**, *6*, 12463–12469.
- (8) Mao, J.; Wang, Y.; Zheng, Z.; Deng, D. The rise of two-dimensional MoS<sub>2</sub> for catalysis. *Front. Phys.* **2018**, *13*, 138118.
- (9) Kumari, S.; Gusain, R.; Kumar, A.; Manwar, N.; Jain, S. L.; Khatri, O. P. Direct growth of nanostructural MoS<sub>2</sub> over the *h*-BN nanoplatelets: an efficient heterostructure for visible light photoreduction of CO<sub>2</sub> to methanol. *J. CO<sub>2</sub> Util.* **2020**, *42*, 101345.
- (10) Li, Y.; Tang, J.; Wei, Y.; He, W.; Tang, Z.; Zhang, X.; Xiong, J.; Zhao, Z. The hetero-junction between 3D ordered macroporous TiO<sub>2</sub> and MoS<sub>2</sub> nanosheets for enhancing visible-light driven CO<sub>2</sub> reduction. *J. CO<sub>2</sub> Util.* **2021**, *51*, 101648.
- (11) Chen, W.; Liu, M.; Wei, S.; Li, X.; Mao, L.; Shangguan, W. Solid-state synthesis of ultrathin MoS<sub>2</sub> as a cocatalyst on mesoporous g-C<sub>3</sub>N<sub>4</sub> for excellent enhancement of visible light photoactivity. *J. Alloys Compd.* **2020**, *836*, 155401.
- (12) Radisavljevic, B.; Radenovic, A.; Brivio, J.; Giacometti, V.; Kis, A. Single-layer MoS<sub>2</sub> transistors. *Nat. Nanotechnol.* **2011**, *6*, 147–150.
- (13) Yuan, H.; Cheng, G.; You, L.; Li, H.; Zhu, H.; Li, W.; Kopanski, J. J.; Obeng, Y. S.; Hight Walker, A. R.; Gundlach, D. J. et al. Influence of metal–MoS<sub>2</sub> interface on MoS<sub>2</sub> transistor performance: comparison of Ag and Ti contacts. *ACS Appl. Mater. Interfaces* **2015**, *7*, 1180–1187.

- (14) van der Zande, A. M.; Huang, P. Y.; Chenet, D. A.; Berkelbach, T. C.; You, Y.; Lee, G.-H.; Heinz, T. F.; Reichman, D. R.; Muller, D. A.; Hone, J. C. Grains and grain boundaries in highly crystalline monolayer molybdenum disulphide. *Nat. Mater.* **2013**, *12*, 554–561.
- (15) Vazirisereshk, M. R.; Martini, A.; Strubbe, D. A.; Baykara, M. Z. Solid lubrication with MoS<sub>2</sub>: a review. *Lubricants* **2019**, *7*, 57.
- (16) Domínguez-Meister, S.; Rojas, T. C.; Brizuela, M.; Sánchez-López, J. C. Solid lubricant behavior of MoS<sub>2</sub> and WSe<sub>2</sub>-based nanocomposite coatings. *Sci. Technol. Adv. Mater.* **2017**, *18*, 122–133.
- (17) Guo, J.; Peng, R.; Du, H.; Shen, Y.; Li, Y.; Li, J.; Dong, G. The application of nano-MoS<sub>2</sub> quantum dots as liquid lubricant additive for tribological behavior improvement. *Nanomaterials* **2020**, *10*, 200.
- (18) Mousavi, S. B.; Heris, S. Z.; Estellé, P. Experimental comparison between ZnO and MoS<sub>2</sub> nanoparticles as additives on performance of diesel oil-based nano lubricant. *Sci. Rep.* **2020**, *10*, 5813.
- (19) Lauritsen, J.; Kibsgaard, J.; Olesen, G.; Moses, P.; Hinnemann, B.; Helveg, S.; Nørskov, J. K.; Clausen, B. S.; Topsøe, H.; Lægsgaard, E. et al. Location and coordination of promoter atoms in Co- and Ni-promoted MoS<sub>2</sub>-based hydrotreating catalysts. *J. Catal.* **2007**, *249*, 220–233.
- (20) Zhang, D.; Wu, J.; Li, P.; Cao, Y. Room-temperature SO<sub>2</sub> gas-sensing properties based on a metal-doped MoS<sub>2</sub> nanoflower: an experimental and density functional theory investigation. *J. Mater. Chem. A* **2017**, *5*, 20666–20677.
- (21) Ko, T.; Huang, C.; Lin, D.; Ruan, Y.; Huang, Y. Electrical and optical properties of Co-doped and undoped MoS<sub>2</sub>. *Jpn. J. Appl. Phys.* **2016**, *55*, 04EP06.

- (22) Xie, Y.; Li, Y. Preparation of Ni-doped MoS<sub>2</sub> microsphere and its superior electrocatalytic hydrogen evolution ability. *Adv. Mater. Res.* **2014**, *871*, 206–210.
- (23) Vellore, A.; Romero Garcia, S.; Walters, N.; Johnson, D.; Kennett, A.; Heverly, M.; Martini, A. Ni-doped MoS<sub>2</sub> dry film lubricant life. *Adv. Mater. Interfaces* **2020**, *7*, 2001109.
- (24) Acikgoz, O.; Guerrero, E.; Yanilmaz, A.; Dagdeviren, O. E.; Çelebi, C.; Strubbe, D. A.; Baykara, M. Z. Intercalation leads to inverse layer dependence of friction on chemically doped MoS<sub>2</sub>. *Nanotechnology* **2023**, *34*, 015706.
- (25) Kong, X.; Wang, N.; Zhang, Q.; Liang, J.; Wang, M.; Wei, C.; Chen, X.; Zhao, Y.; Zhang, X. Ni-doped MoS<sub>2</sub> as an efficient catalyst for electrochemical hydrogen evolution in alkaline media. *ChemistrySelect* **2018**, *3*, 9493–9498.
- (26) Rajendhran, N.; Palanisamy, S.; Periyasamy, P.; Venkatachalam, R. Enhancing of the tribological characteristics of the lubricant oils using Ni-promoted MoS<sub>2</sub> nanosheets as nano-additives. *Tribol. Int.* **2018**, *118*, 314–328.
- (27) Guerrero, E.; Karkee, R.; Strubbe, D. A. Phase stability and Raman/IR signatures of Ni-doped MoS<sub>2</sub> from DFT studies. *J. Phys. Chem. C* **2021**, *125*, 13401–13412.
- (28) Karkee, R.; Guerrero, E.; Strubbe, D. A. Enhanced interlayer interactions in Ni-doped MoS<sub>2</sub>, and structural and electronic signatures of doping site. *Phys. Rev. Materials* **2021**, *5*, 074006.
- (29) Kondekar, N.; Boebinger, M. G.; Tian, M.; Kirmani, M. H.; McDowell, M. T. The effect of nickel on MoS<sub>2</sub> growth revealed with in situ transmission electron microscopy. *ACS Nano* **2019**, *13*, 7117–7126.
- (30) Pan, U. N.; Singh, T. I.; Paudel, D. R.; Gudal, C. C.; Kim, N. H.; Lee, J. H. Covalent doping of Ni and P on 1T-enriched MoS<sub>2</sub> bifunctional 2D-nanostructures with active

- basal planes and expanded interlayers boosts electrocatalytic water splitting. *J. Mater. Chem. A* **2020**, *8*, 19654–19664.
- (31) Jiang, Y.; Li, S.; Zhang, F.; Zheng, W.; Zhao, L.; Feng, Q. Metal-semiconductor 1T/2H-MoS<sub>2</sub> by a heteroatom-doping strategy for enhanced electrocatalytic hydrogen evolution. *Catal. Commun.* **2021**, *156*, 106325.
- (32) Geng, D.; Bo, X.; Guo, L. Ni-doped molybdenum disulfide nanoparticles anchored on reduced graphene oxide as novel electroactive material for a non-enzymatic glucose sensor. *Sens. Actuators B Chem.* **2017**, *244*, 131–141.
- (33) Escalera-López, D.; Niu, Y.; Yin, J.; Cooke, K.; Rees, N. V.; Palmer, R. E. Enhancement of the hydrogen evolution reaction from Ni-MoS<sub>2</sub> hybrid nanoclusters. *ACS Catal.* **2016**, *6*, 6008–6017.
- (34) Wang, D.; Zhang, X.; Shen, Y.; Wu, Z. Ni-doped MoS<sub>2</sub> nanoparticles as highly active hydrogen evolution electrocatalysts. *RSC Adv.* **2016**, *6*, 16656–16661.
- (35) Zhang, J.; Wang, T.; Liu, P.; Liu, S.; Dong, R.; Zhuang, X.; Chen, M.; Feng, X. Engineering water dissociation sites in MoS<sub>2</sub> nanosheets for accelerated electrocatalytic hydrogen production. *Energy Environ. Sci.* **2016**, *9*, 2789–2793.
- (36) Xu, J.; Shao, G.; Tang, X.; Lv, F.; Xiang, H.; Jing, C.; Liu, S.; Dai, S.; Li, Y.; Luo, J. et al. Frenkel-defected monolayer MoS<sub>2</sub> catalysts for efficient hydrogen evolution. *Nat. Commun.* **2022**, *13*, 1–8.
- (37) Dong, T.; Zhang, X.; Wang, P.; Chen, H.-S.; Yang, P. Formation of Ni-doped MoS<sub>2</sub> nanosheets on N-doped carbon nanotubes towards superior hydrogen evolution. *Electrochim. Acta* **2020**, *338*, 135885.
- (38) Khan, M.; Hasan, M.; Bhatti, K.; Rizvi, H.; Wahab, A.; Rehman, S.-u.; Afzal, M. J.; Nazneen, A.; Nazir, A.; Iqbal, M. et al. Effect of Ni doping on the structural, optical

- and photocatalytic activity of MoS<sub>2</sub>, prepared by Hydrothermal method. *Mater. Res. Express* **2020**, *7*, 015061.
- (39) Xuan, N.; Chen, J.; Shi, J.; Yue, Y.; Zhuang, P.; Ba, K.; Sun, Y.; Shen, J.; Liu, Y.; Ge, B. et al. Single-atom electroplating on two dimensional materials. *Chem. Mater.* **2018**, *31*, 429–435.
- (40) Zhang, R.; Dong, Y.; Al-Tahan, M. A.; Zhang, Y.; Wei, R.; Ma, Y.; Yang, C.; Zhang, J. Insights into the sandwich-like ultrathin Ni-doped MoS<sub>2</sub>/rGO hybrid as effective sulfur hosts with excellent adsorption and electrocatalysis effects for lithium-sulfur batteries. *J. Energy Chem.* **2021**, *60*, 85–94.
- (41) Jenisha, M. A.; Kavirajan, S.; Harish, S.; Archana, J.; Kamalabharathi, K.; Kumar, E. S.; Navaneethan, M. Interfacial engineering effect and bipolar conduction of Ni-doped MoS<sub>2</sub> nanostructures for thermoelectric application. *J. Alloys Compd.* **2022**, *895*, 162493.
- (42) Stupp, B. C. Synergistic effects of metals co-sputtered with MoS<sub>2</sub>. *Thin Solid Films* **1981**, *84*, 257–266.
- (43) Rajendhran, N.; Palanisamy, S.; Periyasamy, P.; Venkatachalam, R. Enhancing of the tribological characteristics of the lubricant oils using Ni-promoted MoS<sub>2</sub> nanosheets as nano-additives. *Tribol. Int.* **2018**, *118*, 314–328.
- (44) Zabinski, J. S.; Donley, M. S.; Walck, S. D.; Schneider, T. R.; McDevitt, N. T. The effects of dopants on the chemistry and tribology of sputter-deposited MoS<sub>2</sub> films. *Tribol. Trans.* **1995**, *38*, 894–904.
- (45) Hamilton, M. A.; Alvarez, L. A.; Mauntler, N. A.; Argibay, N.; Colbert, R.; Burris, D. L.; Muratore, C.; Voevodin, A. A.; Perry, S. S.; Sawyer, W. G. A possible link between macroscopic wear and temperature dependent friction behaviors of MoS<sub>2</sub> coatings. *Tribol. Lett.* **2008**, *32*, 91–98.



- (46) Zou, T. Z.; Tu, J. P.; Zhang, S. C.; Chen, L. M.; Wang, Q.; Zhang, L. L.; He, D. N. Friction and wear properties of electroless Ni-P-(IF-MoS<sub>2</sub>) composite coatings in humid air and vacuum. *Mater. Sci. Eng. A* **2006**, *426*, 162–168.
- (47) Wang, H.; Tsai, C.; Kong, D.; Chan, K.; Abild-Pedersen, F.; Nørskov, J.; Cui, Y. Transition-metal doped edge sites in vertically aligned MoS<sub>2</sub> catalysts for enhanced hydrogen evolution. *Nano Res.* **2015**, *8*, 566–575.
- (48) Wei, H.; Gui, Y.; Kang, J.; Wang, W.; Tang, C. A DFT study on the adsorption of H<sub>2</sub>S and SO<sub>2</sub> on Ni doped MoS<sub>2</sub> monolayer. *Nanomaterials* **2018**, *8*, 646.
- (49) Ma, D.; Ju, W.; Li, T.; Zhang, X.; He, C.; Ma, B.; Lu, Z.; Yang, Z. The adsorption of CO and NO on the MoS<sub>2</sub> monolayer doped with Au, Pt, Pd, or Ni: a first-principles study. *Appl. Surf. Sci.* **2016**, *383*, 98–105.
- (50) Raybaud, P.; Hafner, J.; Kresse, G.; Kasztelan, S.; Toulhoat, H. Structure, energetics, and electronic properties of the surface of a promoted MoS<sub>2</sub> catalyst: an ab initio local density functional study. *J. Catal.* **2000**, *190*, 128–143.
- (51) Hao, Y.; Wang, Y.-T.; Xu, L.-C.; Yang, Z.; Liu, R.-p.; Li, X.-y. 1T-MoS<sub>2</sub> monolayer doped with isolated Ni atoms as highly active hydrogen evolution catalysts: a density functional study. *Appl. Surf. Sci.* **2019**, *469*, 292–297.
- (52) Guerrero, E.; Strubbe, D. A. Atomistic Mechanisms of Sliding in Few-Layer and Bulk Doped MoS<sub>2</sub>. *arXiv:2209.15629* **2022**, submitted 30 Sept 2022, <https://doi.org/10.48550/arXiv.2209.15629>.
- (53) Karkee, R.; Strubbe, D. A. Panoply of doping-induced reconstructions and electronic phases in Ni-doped 1T-MoS<sub>2</sub>. *arXiv:2107.07541* **2022**, submitted 11 Mar 2022, <https://doi.org/10.48550/arXiv.2107.07541>.

- (54) Jiang, J.-W.; Park, H. S.; Rabczuk, T. Molecular dynamics simulations of single-layer molybdenum disulphide ( $\text{MoS}_2$ ): Stillinger-Weber parametrization, mechanical properties, and thermal conductivity. *J. Appl. Phys.* **2013**, *114*, 064307.
- (55) Jiang, J.-W.; Zhou, Y.-P. In *Handbook of Stillinger-Weber Potential Parameters for Two-Dimensional Atomic Crystals*; Jiang, J.-W., Zhou, Y.-P., Eds.; IntechOpen: Rijeka, 2017; Chapter 1.
- (56) Ostadhosseini, A.; Rahnamoun, A.; Wang, Y.; Zhao, P.; Zhang, S.; Crespi, V. H.; van Duin, A. C. ReaxFF reactive force-field study of molybdenum disulfide ( $\text{MoS}_2$ ). *J. Phys. Chem. Lett.* **2017**, *8*, 631–640.
- (57) Liu, J.; Zeng, J.; Zhu, C.; Miao, J.; Huang, Y.; Heinz, H. Interpretable molecular models for molybdenum disulfide and insight into selective peptide recognition. *Chem. Sci.* **2020**, *33*, 8708.
- (58) Xing, J.; Shi, H.; Li, Y.; Liu, J. Molecular dynamics study of Cr doping on the crystal structure and surficial/interfacial properties of 2H- $\text{MoS}_2$ . *Phys. Chem. Chem. Phys.* **2022**, *24*, 4547.
- (59) Liang, T.; Phillpot, S. R.; Sinnott, S. B. Parametrization of a reactive many-body potential for Mo–S systems. *Phys. Rev. B* **2009**, *79*, 245110.
- (60) Hong, S.; Krishnamoorthy, A.; Rajak, P.; Tiwari, S.; Misawa, M.; Shimojo, F.; Kalia, R.; Nakano, A.; Vashishta, P. Computational synthesis of  $\text{MoS}_2$  layers by reactive molecular dynamics simulations: initial sulfidation of  $\text{MoO}_3$  surfaces. *Nano Lett.* **2017**, *17*, 4866–4872.
- (61) Chen, R.; Jusufi, A.; Schilowitz, A.; Martini, A. Formation of  $\text{MoS}_2$  from elemental Mo and S using reactive molecular dynamics simulations. *J. Vac. Sci. Technol. A* **2020**, *38*, 022201.

- (62) Ponomarev, I.; Polcar, T.; Nicolini, P. New Reactive Force Field for Simulations of MoS<sub>2</sub> Crystallization. *J. Phys. Chem. C* **2022**, *126*, 9475–9481.
- (63) Chen, R.; Konicek, A. R.; Jusufi, A.; Kliewer, C. E.; Jaishankar, A.; Schilowitz, A.; Martini, A. Limiting domain size of MoS<sub>2</sub>: effects of stoichiometry and oxygen. *J. Phys. Chem. C* **2020**, *124*, 27571–27579.
- (64) Hu, G.; Fung, V.; Sang, X.; Unocic, R. R.; Ganesh, P. Predicting synthesizable multifunctional edge reconstructions in two-dimensional transition metal dichalcogenides. *npj Comput. Mater.* **2020**, *6*, 1–9.
- (65) Yilmaz, D. E.; Lotfi, R.; Ashraf, C.; Hong, S.; van Duin, A. C. Defect design of two-dimensional MoS<sub>2</sub> structures by using a graphene layer and potato stamp concept. *J. Phys. Chem. C* **2018**, *122*, 11911–11917.
- (66) Noori, H.; Mortazavi, B.; Keshtkari, L.; Zhuang, X.; Rabczuk, T. Nanopore creation in MoS<sub>2</sub> and graphene monolayers by nanoparticles impact: a reactive molecular dynamics study. *Appl. Phys. A* **2021**, *127*, 1–13.
- (67) Patra, T. K.; Zhang, F.; Schulman, D. S.; Chan, H.; Cherukara, M. J.; Terrones, M.; Das, S.; Narayanan, B.; Sankaranarayanan, S. K. Defect dynamics in 2-D MoS<sub>2</sub> probed by using machine learning, atomistic simulations, and high-resolution microscopy. *ACS Nano* **2018**, *12*, 8006–8016.
- (68) Zahedi, R. K.; Alajlan, N.; Zahedi, H. K.; Rabczuk, T. Mechanical properties of all MoS<sub>2</sub> monolayer heterostructures: crack propagation and existing notch study. *Comput. Mater. Contin.* **2022**, *70*, 4635–4655.
- (69) Mejía-Rosales, S.; Sandoval-Salazar, S. A.; Soria-Sánchez, A.; Cantú-Sánchez, L. Y. Mechanical properties of MoS<sub>2</sub> nanotubes under tension: a molecular dynamics study. *Mol. Simul.* **2021**, *47*, 471–479.

- (70) Mortazavi, B.; Ostadhossein, A.; Rabczuk, T.; Van Duin, A. C. Mechanical response of all-MoS<sub>2</sub> single-layer heterostructures: a ReaxFF investigation. *Phys. Chem. Chem. Phys.* **2016**, *18*, 23695–23701.
- (71) Shi, Y.; Cai, Z.; Pu, J.; Wang, L.; Xue, Q. Interfacial molecular deformation mechanism for low friction of MoS<sub>2</sub> determined using ReaxFF-MD simulation. *Ceram. Int.* **2019**, *45*, 2258–2265.
- (72) Giannozzi, P.; Andreussi, O.; Brumme, T.; Bunau, O.; Buongiorno Nardelli, M.; Calandra, M.; Car, R.; Cavazzoni, C.; Ceresoli, D.; Cococcioni, M. et al. Advanced capabilities for materials modelling with QUANTUM ESPRESSO. *J. Phys. Condens. Matter* **2017**, *29*, 465901.
- (73) Perdew, J. P.; Burke, K.; Ernzerhof, M. Generalized Gradient Approximation made simple. *Phys. Rev. Lett.* **1996**, *77*, 3865–3868.
- (74) Grimme, S. Semiempirical GGA-type density functional constructed with a long-range dispersion correction. *J. Comput. Chem.* **2006**, *27*, 1787–1799.
- (75) Hamann, D. R. Optimized norm-conserving Vanderbilt pseudopotentials. *Phys. Rev. B* **2013**, *88*, 085117.
- (76) Schlipf, M.; Gygi, F. Optimization algorithm for the generation of ONCV pseudopotentials. *Comput. Phys. Commun.* **2015**, *196*, 36–44.
- (77) van Duin, A. C.; Dasgupta, S.; Lorant, F.; Goddard, W. A. ReaxFF: a reactive force field for hydrocarbons. *J. Phys. Chem. A* **2001**, *105*, 9396–9409.
- (78) Vasenkov, A.; Newsome, D.; Verners, O.; Russo Jr, M. F.; Zaharieva, R.; Van Duin, A. C. Reactive molecular dynamics study of Mo-based alloys under high-pressure, high-temperature conditions. *J. Appl. Phys.* **2012**, *112*, 013511.

- (79) Chen, H.-P.; Kalia, R. K.; Kaxiras, E.; Lu, G.; Nakano, A.; Nomura, K.-i.; Van Duin, A. C.; Vashishta, P.; Yuan, Z. Embrittlement of metal by solute segregation-induced amorphization. *Phys. Rev. Lett.* **2010**, *104*, 155502.
- (80) van Duin, A. C.; Baas, J. M.; Van De Graaf, B. Delft molecular mechanics: a new approach to hydrocarbon force fields. Inclusion of a geometry-dependent charge calculation. *J. Chem. Soc., Faraday Trans.* **1994**, *90*, 2881–2895.
- (81) Mueller, J. E.; van Duin, A. C.; Goddard III, W. A. Development and validation of ReaxFF reactive force field for hydrocarbon chemistry catalyzed by nickel. *J. Phys. Chem. C* **2010**, *114*, 4939–4949.
- (82) Hahn, S. H.; Rimsza, J.; Criscenti, L.; Sun, W.; Deng, L.; Du, J.; Liang, T.; Sinnott, S. B.; Van Duin, A. C. Development of a ReaxFF reactive force field for NaSiO<sub>x</sub>/water systems and its application to sodium and proton self-diffusion. *J. Phys. Chem. C* **2018**, *122*, 19613–19624.
- (83) Nayir, N.; Van Duin, A. C.; Erkoc, S. Development of the Reaxff reactive force field for inherent point defects in the Si/silica system. *J. Phys. Chem. A* **2019**, *123*, 4303–4313.
- (84) Khajeh, A.; Hu, X.; Mohammadtabar, K.; Shin, Y.; van Duin, A. C. .; Berkebile, S.; Martini, A. Statistical analysis of tri-cresyl phosphate conversion on an iron oxide surface using reactive molecular dynamics simulations. *J. Phys. Chem. C* **2019**, *123*, 12886–12893.
- (85) Plimpton, S. Fast parallel algorithms for short-range molecular dynamics. *J. Comput. Phys.* **1995**, *117*, 1–19.
- (86) Zhou, W.; Zou, X.; Najmaei, S.; Liu, Z.; Shi, Y.; Kong, J.; Lou, J.; Ajayan, P. M.; Yakobson, B. I.; Idrobo, J.-C. Intrinsic structural defects in monolayer molybdenum disulfide. *Nano Lett.* **2013**, *13*, 2615–2622.

- (87) Sirota, B.; Glavin, N.; Voevodin, A. A. Room temperature magnetron sputtering and laser annealing of ultrathin MoS<sub>2</sub> for flexible transistors. *Vacuum* **2019**, *160*, 133–138.
- (88) Taguchi, M.; Hamaguchi, S. MD simulations of amorphous SiO<sub>2</sub> thin film formation in reactive sputtering deposition processes. *Thin Solid Films* **2007**, *515*, 4879–4882.
- (89) Grigoriev, F. V.; Sulimov, A. V.; Kochikov, I.; Kondakova, O. A.; Sulimov, V. B.; Tikhonravov, A. V. High-performance atomistic modeling of optical thin films deposited by energetic processes. *Int. J. High Perform. Comput. Appl.* **2015**, *29*, 184–192.
- (90) McConney, M. E.; Glavin, N. R.; Juhl, A. T.; Check, M. H.; Durstock, M. F.; Voevodin, A. A.; Shelton, T. E.; Bultman, J. E.; Hu, J.; Jespersen, M. L. et al. Direct synthesis of ultra-thin large area transition metal dichalcogenides and their heterostructures on stretchable polymer surfaces. *J. Mater. Res.* **2016**, *31*, 967–974.
- (91) Scharf, T. W.; Goeke, R. S.; Kotula, P. G.; Prasad, S. V. Synthesis of Au-MoS<sub>2</sub> nanocomposites: thermal and friction-induced changes to the structure. *ACS Appl. Mater. Interfaces* **2013**, *5*, 11762–11767.

# TOC Graphic

